

Resolving the trap levels of Se and $\text{Se}_{1-x}\text{Te}_x$ via deep-level transient spectroscopyXin Chen, Songxue Bai, Ruiming Li, Yujie Yang, and Qianqian Lin **Key Lab of Artificial Micro- and Nano-Structures of Ministry of Education of China, Hubei Luoqia Laboratory, School of Physics and Technology, Wuhan University, Wuhan, Hubei 430072, People's Republic of China*

(Received 31 December 2023; accepted 12 March 2024; published 28 March 2024)

Benefiting from the facile fabrication and tunable optoelectronic properties, Se and $\text{Se}_{1-x}\text{Te}_x$ are promising candidates for optoelectronic applications, e.g., thin film solar cells and short-wavelength infrared detectors. However, the trap features of selenium based semiconductors are complicated mainly due to the low crystallinity induced dispersive nature. In particular, the underlying charge transport properties of $\text{Se}_{1-x}\text{Te}_x$ have not been systematically investigated, which is crucial for device optimization in real applications. In this work, we first introduce deep-level transient spectroscopy to characterize Se and Se-based semiconductors, and we also compare it with reverse-bias deep-level transient spectroscopy. It was found that the latter technique can result in much higher transient capacitance signal and better energy resolution. Based on the full analysis of the transient capacitance, we found the introduction of Te into Se can easily form two additional deep trap states around 0.55 eV and 0.75 eV, respectively, and it also explains why the device performance of $\text{Se}_{1-x}\text{Te}_x$ are still suffering from the large dark current and recombination losses.

DOI: [10.1103/PhysRevMaterials.8.033805](https://doi.org/10.1103/PhysRevMaterials.8.033805)

I. INTRODUCTION

Selenium (Se) is one of the most traditional semiconductor materials used in optoelectronic devices [1,2]. The fabrication process of selenium-based solar cells is facile and can be prepared at low temperature. In addition, it is environmentally friendly and has excellent stability. This makes it possible to mass-produce selenium-based solar cells at ultralow cost. For instance, Li *et al.* fabricated highly efficient Se solar cells based on a two-step melting process (TSMP) [3], and Todorov *et al.* achieved the efficiency of 6.5% by optimizing the thickness of the functional layers and employing a MoO_x hole-transport layer [4]. However, the bandgap of selenium is 1.8 ~ 2.0 eV [5,6], which is larger than the optimal bandgap of single-junction photovoltaic devices (1~1.5 eV). This limits the further improvement of the efficiency of Se solar cells. More recently, pristine Se was mixed with narrow-bandgap (0.33 eV) [7] semiconductor material-Te to form $\text{Se}_{1-x}\text{Te}_x$ alloy, resulting in a smaller and tunable bandgap, which may help to overcome the Shockley-Queisser limit [8–10]. Meanwhile, selenium can also be used as an excellent photodetector material. Some of the commercial X-ray imaging chips are currently made of amorphous selenium [11–13]. Recently, short-wave infrared (SWIR) photodetectors based on $\text{Se}_{1-x}\text{Te}_x$ alloys have also been reported. For instance, Fu *et al.* fabricated low-cost, high-performance, and highly stable $\text{Se}_{1-x}\text{Te}_x$ short-wave infrared photodetectors through low-temperature evaporation and post-annealing processes [14]. Li *et al.* have also realized highly sensitive, ultrafast photodiodes by careful tuning the composition and charge carrier dynamics of $\text{Se}_{1-x}\text{Te}_x$ alloys [15].

Another critical factor affecting device performance is the trap features. Based on the energy level, trap states can be divided into shallow level trap states and deep level trap states [16]. Shallow level trap states are located near the band edge, while deep level trap states are typically located in the middle of the forbidden band. Particularly, deep level trap states pose the greatest threat to device performance. Due to the high activation energy of deep level trap states, carriers are difficult to be re-emitted at room temperature once they are captured by these deep states. Therefore, such trap states will become an effective recombination center, resulting in serious nonradiative recombination [17]. It is well recognized in the field that nonradiative recombination losses are the killer of open-circuit voltage (V_{OC}) of solar cells and reduce the power conversion efficiency (PCE) remarkably [18]. In addition, trap states can also act as the main reaction active sites of water and oxygen [19–22], affecting the stability of devices. In some circumstances, trap states can also influence the charge transport significantly, and can be utilized for specific applications, e.g., the filterless narrowband photodiodes [23]. Hence, precisely characterizing and modulating the trap features are of great importance for designing high-performance optoelectronic devices. However, the characterizing of deep level traps is extremely challenging. There is currently little research on trap states in Se and $\text{Se}_{1-x}\text{Te}_x$ alloys, especially on deep level trap states. It is worth mentioning that multiple energy levels of defects may exist in $\text{Se}_{1-x}\text{Te}_x$ alloys, which will bring additional difficulties to the characterization of their trap information.

To solve the above issues, we introduce deep level transient spectroscopy (DLTS) to study the defect features of operational Se-based photodiodes. DLTS is one of the most powerful transient capacitance probe for measuring deep level traps in semiconductor devices, which was proposed by Lang in 1974 [24]. DLTS can effectively record the

*q.lin@whu.edu.cn

capture and reemission processes of charge carriers by the trap state. Benefiting from its extremely high sensitivity and wide detection range, it has been widely used for the characterization of defects in traditional semiconductors. Through DLTS testing technology, we can obtain information such as trap type, concentration, activation energy, and capture cross section [25–27]. In this work, we also introduce reverse bias deep level transient spectroscopy (RDLTS) to conduct a detailed study of Se and $\text{Se}_{1-x}\text{Te}_x$ semiconductors. Compared with DLTS, RDLTS more focuses on the carrier capture process [28,29], normally has stronger signal and better energy resolution [28]. Combining both techniques, it is expected to resolve the complex energy levels of Se based semiconductors, and reveal the effect of Te composition on the trap features of $\text{Se}_{1-x}\text{Te}_x$ alloy.

II. RESULTS AND DISCUSSION

Both Se and $\text{Se}_{1-x}\text{Te}_x$ thin films were prepared by thermal evaporation, and all the samples were deposited on glass substrates or indium tin oxide (ITO) transparent electrodes (see the Supplemental Material [30] for more details). The prepared thin films are uniform and the thickness can be easily modulated by the evaporation rate and deposition time. Figure S1 (see the Supplemental Material [30]) displays the typical transmittance, reflectance, and reflectance-corrected absorption spectra. With the increase of Te content, the absorption edge of the $\text{Se}_{1-x}\text{Te}_x$ thin films shifted to the infrared region, suggesting a reduced bandgap, which is in line with the literature [15]. To validate the techniques used in this work, we first evaluated the pristine Se-based devices with a structure of ITO/SnO₂/Active layer/Sb, and the active layer is composed of $\text{Se}_{1-x}\text{Te}_x$ alloy, with x varied from zero to one. Figure S2 [30] schematically illustrates the device structure used in this work. Figure 1(a) depicts the typical current density-voltage (J - V) curves of the Se-based photodiodes both in the dark and under one sun illumination (100 mW/cm²). The devices showed decent rectifying characteristics and relatively low dark current (<1 μA in the testing region). The capacitance-voltage (C - V) curves [Fig. 1(b)] also exhibited a typical bias dependent junction capacitance, resulting in a built-in field of ~ 0.7 V, which is solid evidence suggesting the formation of decent PN junctions between the P-type $\text{Se}_{1-x}\text{Te}_x$ active layer and N-type SnO₂ layer. In addition, we also determined the energy levels of the pristine Se layer as shown in Fig. S3 [30], which again confirmed the P-type feature of Se-based semiconductor. Figures 1(c) and 1(d) present the recorded transient capacitance decays at various temperatures of DLTS and RDLTS measurements. The variations of transient capacitance in the emission process can be governed by

$$\Delta C(t) = \Delta C_{\max} e^{e_T(t-t_0)}, \quad (1)$$

where t_0 is the start time to record the transient capacitance decays. ΔC_{\max} is the maximal change of capacitance when removing the filling pulse. Then, the mission rate (e_T) can be extracted from the transient decays. It is worth noting that e_T is highly temperature dependent, given by

$$e_T = N_{c,v} \sigma_c v_{th} e^{-\frac{E_a}{kT}}, \quad (2)$$

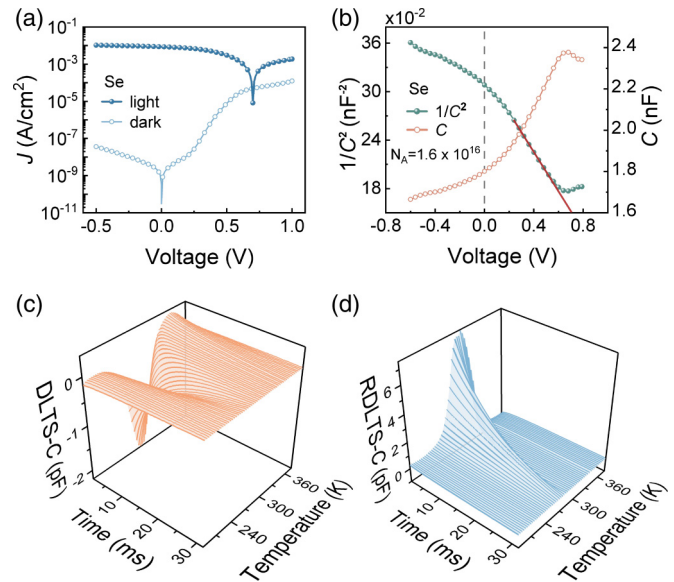


FIG. 1. (a) J - V curves of Se-based photodiode measured in the dark and under 100 mW/cm²; (b) C - V curves of Se-based photodiode, recorded transient capacitance decays of Se-based photodiode at various temperature based on (c) DLTS and (d) RDLTS measurements.

where σ_c is the trap capture cross section, E_a is the activation energy of the trap state, and $N_{c,v}$ is the carrier density in the conduction band or valence band for electron and hole traps, respectively. In addition, another crucial parameter is the trap concentration (N_T), which is proportional to the amplitude of the DLTS signal. This implies that the trap concentration can be directly obtained from the transient change in capacitance, given by

$$N_T = \frac{2\Delta C_{\max}}{C_R} N_A, \quad (3)$$

where N_T is the trap concentration, C_R is the static capacitance value under reverse bias voltage, and N_A is the concentration of shallow trap states. Furthermore, DLTS can also distinguish the types of defect induced traps. For ideal point defects, their activation energy is hardly affected by the pulse width, that is, the DLTS signal peak temperature does not change with the variation in pulse width [31,32]. For extended defects, they form deep one-dimensional bands rather than isolated levels. The filling degree of extended defects varies with different pulse widths, leading to different activation energies. Therefore, the DLTS signal peak temperature is highly dependent on pulse width for extended defects, given by [31,33,34]

$$\Delta C_{\text{Amp}} \propto \ln(t_p), \quad (4)$$

where C_{Amp} denotes the amplitude of the DLTS signal, and t_p is the pulse width. Here, we conducted DLTS and RDLTS measurements on pristine Se samples. Compared with DLTS, the transient capacitance signal obtained from RDLTS was much higher, and the amplitude also changed sign as DLTS used a forward bias voltage pulse and the RDLTS used a voltage pulse at reverse bias. All of these transient capacitance curves showed more or less single exponential decays, indicating a single trap state existed in Se thin films. In addition,

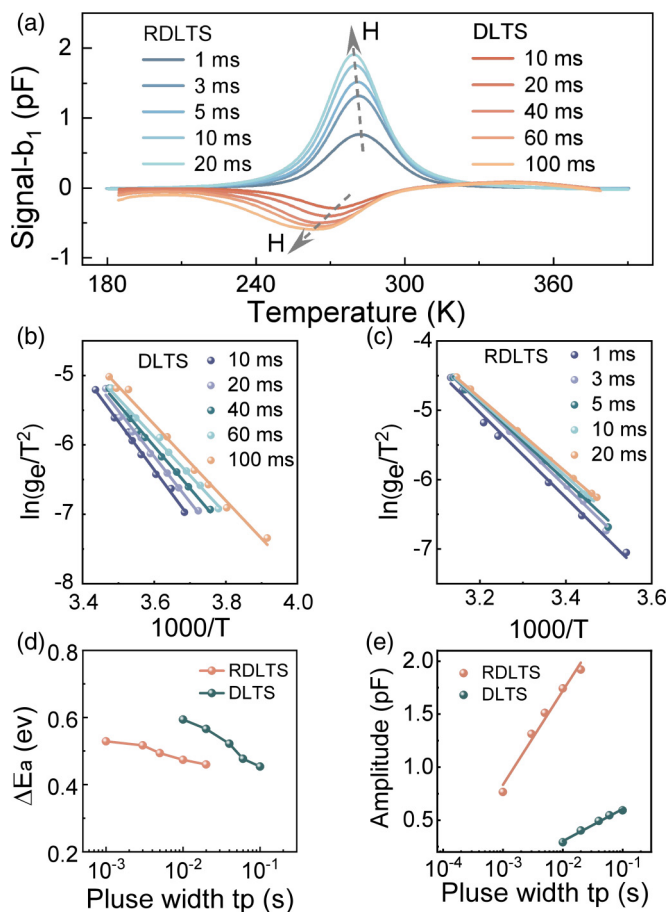


FIG. 2. (a) Comparison of DLTS and RDLTS spectra of Se-based photodiodes at various pulse filling widths, and the label “H” represents the hole traps. Arrhenius plots of the emission rates as a function of $1/T$ of (b) DLTS and (c) RDLTS measurements, and (d) the comparison of retrieved activation energy. (e) Pulse width dependent amplitude of DLTS measurement.

the RDLTS also showed a sharper signal at around 300 K, which suggests the energy resolution of RDLTS could be better, as the devices are the same for both DLTS and RDLTS measurement.

Furthermore, we plotted the DLTS and RDLTS signals versus temperature as shown in Fig. 2(a). It is more evident that the emission of trapped carriers resulted in a much sharper and stronger signal from the RDLTS measurement. In addition, the signal also increased with the increase of filling pulse widths, which has the similar trend as DLTS. However, DLTS measurement requires relatively longer filling pulses compared with RDLTS. By fitting the Arrhenius plot of emission rate as a function of the $1/T$, we can further extract the energy level of the hole trap state (H1) at various filling pulse widths as shown in Figs. 2(b) and 2(c). The determined activation energy (ΔE_a) of the trap state of Se from DLTS and RDLTS is shown in Fig. 2(d). Interestingly, the RDLTS showed less pulse width dependent activation energy, and the value retrieved from DLTS was more dispersive. Again, it confirmed the point that RDLTS has better energy resolution for determining the trap levels. Moreover, we also fitted the amplitude of the DLTS and RDLTS as a function of filling

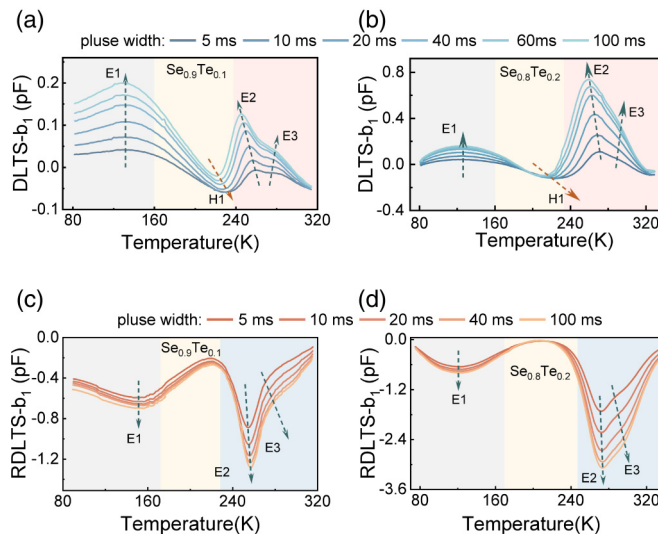


FIG. 3. DLTS spectra of (a) $Se_{0.9}Te_{0.1}$ and (b) $Se_{0.8}Te_{0.2}$ based photodiodes. RDLTS spectra of (c) $Se_{0.9}Te_{0.1}$ and (d) $Se_{0.8}Te_{0.2}$ based photodiodes. The labels “E1,” “E2,” and “E3” represent the electron traps.

pulse width, and found a linear dependency in Fig. 2(e), suggesting the trap states are caused by extended defects instead of pointlike defects. Based on the characterization of a relative pristine sample Se, it has been confirmed that both RDLTS and DLTS are capable to characterize the trap states of Se-based semiconductors with almost the same results and slightly different features.

Having established the techniques, we now move to more complex samples, that is the $Se_{1-x}Te_x$ alloy. Compared with pristine Se, Te has a much lower bandgap and can easily cause deep trap states within the $Se_{1-x}Te_x$ alloy. However, how Te affects the formation of trap states is not clear and has not been studied systematically. In the following study, we focus on the $Se_{1-x}Te_x$ thin film based devices with small Te contents of 10% and 20%, respectively. We also fabricated similar photodiodes as Se, and show their J - V and C - V curves in Fig. S4 [30]. The devices showed slightly increased dark current and reduced build-in field compared with Se-based photodiodes. However, these $Se_{1-x}Te_x$ alloy based devices are still good enough for DLTS measurements. Hence, we recorded their transient capacitance decays as shown in Fig. S5 [30]. With the addition of Te, the trap features of Se-based semiconductors changed profoundly.

We noted that both samples showed multiple electron traps (i.e., E1, E2, and E3) as shown in Fig. 3. Compared with $Se_{0.9}Te_{0.1}$, $Se_{0.8}Te_{0.2}$ sample showed stronger E2 and E3, and the energy levels were hard to be distinguished. Hence, we also characterized these $Se_{1-x}Te_x$ -based devices with RDLTS as shown in Figs. 3(c) and 3(d). Interestingly, we observed similar trap features compared with DLTS data. However, the emission peak of E1 was relatively weak, but the E2 and E3 peaks are relatively strong and sharp. It suggests that E2 and E3 are more sensitive to RDLTS testing, which could be more related to the trap states spatially close to the interfaces, as the depletion region was increased at reverse bias condition [35,36]. From Fig. 3, it can be observed that E2 and E3

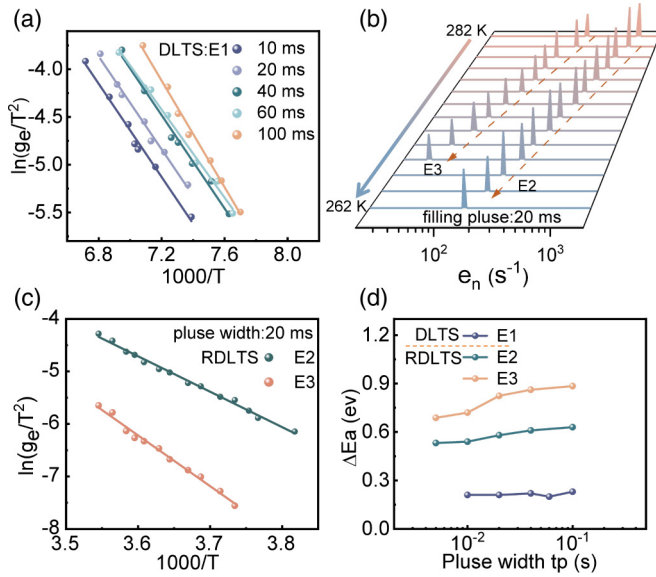


FIG. 4. (a) Arrhenius plot of the emission rates of E1 extracted from DLTS as a function of $1/T$, (b) Laplace-RDLTS spectra of $\text{Se}_{0.9}\text{Te}_{0.1}$ -based photodiodes, (c) Arrhenius plot of the emission rates of E2 and E3 extracted from RDLTS as a function of $1/T$, and (d) obtained activation energy of all traps extracted both from DLTS and RDLTS.

exhibit stronger signal in $\text{Se}_{0.8}\text{Te}_{0.2}$ compared with $\text{Se}_{0.9}\text{Te}_{0.1}$. This indicates that the concentration of E2 and E3 traps is also related to the Te content in $\text{Se}_{1-x}\text{Te}_x$. Table S1 [30] summarizes specific concentration values of E1, E2, and E3 traps under DLTS and RDLTS testing for the maximum pulse width ($t_p=100$ ms).

To further elucidate the trap information, we carefully analyzed the RDLTS and DLTS data obtained from the $\text{Se}_{0.9}\text{Te}_{0.1}$ -based photodiodes. We carefully extracted the activation energy based on the Arrhenius plot of the emission rates of discrete level E1 obtained from DLTS measurements [Fig. 4(a)]. For overlapped E2 and E3 trap levels, we analyzed the recorded capacitance transients by using an inverse Laplace transform, which offers much higher spectral resolution and a possibility of distinguishing closely spaced trap levels [37,38]. The typical Laplace-RDLTS spectra are shown in Fig. 4(b) measured with a pulse width of 20 ms. We also calculated similar spectra with variable pulse widths as shown in Fig. S6 [30]. The emission peaks can be clearly observed

from the Laplace-RDLTS spectra. Based on the temperature dependency, we can further extract the activation energy based on the Arrhenius plots as shown in Fig. 4(c) and 4(d), respectively. Figure S7 [30] further displays the Arrhenius plots of emission rates as a function of $1000/T$ measured at various filling pulse widths. It is worth mentioning that the extracted energy levels of electron trap states E1 and E2 of $\text{Se}_{0.9}\text{Te}_{0.1}$ are less pulse width dependent. E3 has slight pulse width dependency. Compared with E2 (~ 0.55 eV) and E3 (~ 0.75 eV), E1 is relatively shallow (~ 0.2 eV), and should have less impact on the device performance. In Fig. 3, we also observed several anomalous behaviors of the hole trap H1 from the DLTS measurement. However, the H1 peak is prominent in RDLTS. In addition, the shape of the H1 peak was highly distorted, affected by the E2 trap state, especially for longer pulse width. Therefore, we performed DLTS testing with a short pulse ($t_p=1$ ms) and obtained a well-defined H1 peak (Fig. S8 [30]). By constructing the Arrhenius plot, we determined its activation energy to be 0.47 eV, which falls within the range of activation energies for hole traps in pristine Se.

III. CONCLUSION

In summary, we systematically investigated the trap features of Se and $\text{Se}_{1-x}\text{Te}_x$ alloys combining both DLTS and RDLTS, which are transient capacitance techniques. Based on the full analysis of the obtained DLTS spectra, we extracted the energy levels of these Se based semiconductors, and revealed the impact of Te on the formation of deep electron traps. Technically, RDLTS has stronger signal and requires short pulse width, and exhibits much better energy resolution. DLTS has better sensitivity to relative shallow, discrete trap states. Combining both benefits, we successfully resolved the complicated energy levels of the $\text{Se}_{1-x}\text{Te}_x$ thin films based on operational devices, implying that DLTS could be a powerful technique to characterize Se-based semiconductors.

ACKNOWLEDGMENTS

This work was financially supported by the National Natural Science Foundation of China (Grant No. 61875154), Wuhan Science and Technology Bureau (Grant No. 2022010801010108), and the project supported by the open fund of Hubei Luojia Laboratory (Grant No. 220100042). We thank the Core Facility of Wuhan University for the access to analytical equipment.

[1] C. E. Fritts, On a new form of selenium cell, and some electrical discoveries made by its use, *Am. J. Sci.* **26**, 465 (1883).
 [2] I. Hadar, T.-B. Song, W. Ke, and M. G. Kanatzidis, Modern processing and insights on selenium solar cells: the world's first photovoltaic device, *Adv. Energy Mater.* **9**, 1802766 (2019).
 [3] J. W. Wu, Z. H. Zhang, C. H. Tong, D. Y. Li, A. Y. Mei *et al.*, Two-stage melt processing of phase-pure selenium for printable triple-mesoscopic solar cells, *ACS Appl. Mater. Interfaces* **11**, 33879 (2019).
 [4] T. K. Todorov, S. Singh, D. M. Bishop, O. Gunawan, Y. S. Lee *et al.*, Ultrathin high band gap solar cells with improved

efficiencies from the world's oldest photovoltaic material, *Nat. Commun.* **8**, 682 (2017).
 [5] A. K. Bhatnagar, K. V. Reddy, and V. Srivastava, Optical-energy gap of amorphous selenium - effect of annealing, *J. Phys. D: Appl. Phys.* **18**, L149 (1985).
 [6] S. Tutihasi and I. Chen, Optical properties and band structure of trigonal selenium, *Phys. Rev.* **158**, 623 (1967).
 [7] V. Anzin, M. Eremets, Y. V. Koshichkin, A. Nadezhdinskii, and A. Shirokov, Measurement of the energy gap in tellurium under pressure, *Phys. Status Solidi A* **42**, 385 (1977).

- [8] S. S. Hegedus and W. N. Shafarman, Thin-film solar cells: device measurements and analysis, *Prog. Photovolt.* **12**, 155 (2004).
- [9] Q. Q. Lin, Z. P. Wang, H. J. Snaith, M. B. Johnston, and L. M. Herz, Hybrid perovskites: prospects for concentrator solar cells, *Adv. Sci.* **5**, 1700792 (2018).
- [10] U. Rau and J. H. Werner, Radiative efficiency limits of solar cells with lateral band-gap fluctuations, *Appl. Phys. Lett.* **84**, 3735 (2004).
- [11] H. Huang and S. Abbaszadeh, Recent developments of amorphous selenium-based X-ray detectors: a review, *IEEE Sens. J.* **20**, 1694 (2019).
- [12] S. Kasap, J. B. Frey, G. Belev, O. Tousignant, H. Mani *et al.*, Amorphous selenium and its alloys from early xeroradiography to high resolution X-ray image detectors and ultrasensitive imaging tubes, *Phys. Status Solidi B* **246**, 1794 (2009).
- [13] J. A. Rowlands, W. Zhao, I. M. Blevis, D. F. Waechter, and Z. Huang, Flat-panel digital radiology with amorphous selenium and active-matrix readout, *Radiographics* **17**, 753 (1997).
- [14] L. Fu, Y. He, J. Zheng, Y. Hu, J. Xue *et al.*, $\text{Te}_x\text{Se}_{1-x}$ photodiode shortwave infrared detection and imaging, *Adv. Mater.* **35**, 2211522 (2023).
- [15] R. Li, F. Yao, Y. Xu, S. Bai, Z. Jia, and Q. Lin, Optimizing the charge carrier dynamics of thermal evaporated $\text{Te}_x\text{Se}_{1-x}$ films for high-performance short-wavelength infrared photodetection, *Adv. Funct. Mater.* **34**, 2307005 (2024).
- [16] L. Fu, H. Li, L. Wang, R. Yin, B. Li *et al.*, Defect passivation strategies in perovskites for an enhanced photovoltaic performance, *Energy Environ. Sci.* **13**, 4017 (2020).
- [17] Z. G. Xiao, Y. B. Yuan, Q. Wang, Y. C. Shao, Y. Bai *et al.*, Thin-film semiconductor perspective of organometal trihalide perovskite materials for high-efficiency solar cells, *Mater. Sci. Eng. R: Rep.* **101**, 1 (2016).
- [18] Y. Li, W. Li, Y. Xu, R. Li, T. Yu *et al.*, Interfacial engineering of perovskite solar cells with evaporated PbI_2 ultrathin layers, *ACS Appl. Mater. Interfaces* **13**, 53282 (2021).
- [19] N. Ahn, K. Kwak, M. S. Jang, H. Yoon, B. Y. Lee *et al.*, Trapped charge-driven degradation of perovskite solar cells, *Nat. Commun.* **7**, 13422 (2016).
- [20] N. Aristidou, C. Eames, I. Sanchez-Molina, X. Bu, J. Kosco *et al.*, Fast oxygen diffusion and iodide defects mediate oxygen-induced degradation of perovskite solar cells, *Nat. Commun.* **8**, 15218 (2017).
- [21] N. Aristidou, I. Sanchez-Molina, T. Chotchuangchutchaval, M. Brown, L. Martinez *et al.*, The role of oxygen in the degradation of methylammonium lead trihalide perovskite photoactive layers, *Angew. Chem.-Int. Edit.* **54**, 8208 (2015).
- [22] A. M. Leguy, Y. Hu, M. Campoy-Quiles, M. I. Alonso, O. J. Weber *et al.*, Reversible hydration of $\text{CH}_3\text{NH}_3\text{PbI}_3$ in films, single crystals, and solar cells, *Chem. Mater.* **27**, 3397 (2015).
- [23] Y. Xu, R. Li, S. Bai, Y. Li, Z. Jia *et al.*, Chalcogenide-based narrowband photodetectors for imaging and light communication, *Adv. Funct. Mater.* **33**, 2212523 (2023).
- [24] D. Lang, Deep-level transient spectroscopy: a new method to characterize traps in semiconductors, *J. Appl. Phys.* **45**, 3023 (1974).
- [25] W. Lian, C. Jiang, Y. Yin, R. Tang, G. Li *et al.*, Revealing composition and structure dependent deep-level defect in antimony trisulfide photovoltaics, *Nat. Commun.* **12**, 3260 (2021).
- [26] E. Omotoso, A. T. Paradzah, E. Igumbor, B. Taleatu, W. E. Meyer *et al.*, Determination of capture barrier energy of the E-center in palladium Schottky barrier diodes of antimony-doped germanium by varying the pulse width, *Mater. Res. Express* **7**, 025901 (2020).
- [27] Y. Zhao, M. Tripathi, K. Cernevics, A. Avsar, H. G. Ji *et al.*, Electrical spectroscopy of defect states and their hybridization in monolayer MoS_2 , *Nat. Commun.* **14**, 44 (2023).
- [28] M. Igalson and P. Zabierowski, Transient capacitance spectroscopy of defect levels in CIGS devices, *Thin Solid Films* **361**, 371 (2000).
- [29] Y. B. Jia and H. G. Grimmeiss, Electrical-field dependence of the emission properties of DX-related centers in algaas, *Semicond. Sci. Technol.* **9**, 356 (1994).
- [30] See Supplemental Material at <http://link.aps.org/supplemental/10.1103/PhysRevMaterials.8.033805> for a detailed description of preparation methods and supplemental figures.
- [31] L. Gelczuk, M. Dabrowska-Szata, and G. Jóźwiak, Distinguishing and identifying point and extended defects in DLTS measurements, *Mater. Sci.-Pol.* **23**, 625 (2005).
- [32] S. Heo, J. Chung, H.-I. Lee, J. Lee, J.-B. Park *et al.*, Defect visualization of $\text{Cu}(\text{InGa})(\text{SeS})_2$ thin films using DLTS measurement, *Sci. Rep.* **6**, 30554 (2016).
- [33] P. N. Grillot, S. A. Ringel, E. A. Fitzgerald, G. P. Watson, and Y. H. Xie, electron trapping kinetics at dislocations in relaxed $\text{Ge}_{0.3}\text{Si}_{0.7}/\text{Si}$ heterostructures, *J. Appl. Phys.* **77**, 3248 (1995).
- [34] E. Zielony, K. Olender, E. Placzek-Popko, T. Wosinski, A. Racino *et al.*, Electrical and photovoltaic properties of CdTe/ZnTe n-i-p junctions grown by molecular beam epitaxy, *J. Appl. Phys.* **115**, 244501 (2014).
- [35] F. Lu, D. W. Gong, H. H. Sun, and X. Wang, detection of defects at homoepitaxial interface by deep-level transient spectroscopy, *J. Appl. Phys.* **77**, 213 (1995).
- [36] A. S. Shikoh, A. Y. Polyakov, P. Gostishchev, D. S. Saranin, I. V. Shchemerov *et al.*, On the relation between mobile ion kinetics, device design, and doping in double-cation perovskite solar cells, *Appl. Phys. Lett.* **118**, 093501 (2021).
- [37] I. Capan, T. Brodar, Z. Pastuović, R. Siegele, T. Ohshima *et al.*, Double negatively charged carbon vacancy at the h-and k-sites in 4H-SiC: Combined Laplace-DLTS and DFT study, *J. Appl. Phys.* **123**, 161597 (2018).
- [38] L. Dobaczewski, P. Kaczor, I. Hawkins, and A. Peaker, Laplace transform deep-level transient spectroscopic studies of defects in semiconductors, *J. Appl. Phys.* **76**, 194 (1994).